



Cite this: *RSC Adv.*, 2019, 9, 23334

TiO₂@Sn₃O₄ nanorods vertically aligned on carbon fiber papers for enhanced photoelectrochemical performance

Weiwei Xia,^{†a} Haoyu Qian,^{†a} Xianghua Zeng,^{ab} Jiawei Sun,^a Pengdi Wang,^a Min Luo^a and Jing Dong^a

Semiconductor heterostructures are regarded as an efficient way to improve the photocurrent in photoelectrochemical cell-type (PEC) photodetectors. To better utilize solar energy, TiO₂@Sn₃O₄ arrays vertically aligned on carbon fiber papers were synthesized *via* a hydrothermal route with a two-step method and used as photoanodes in a self-powered photoelectrochemical cell-type (PEC) photodetector under visible light. TiO₂@Sn₃O₄ heterostructures exhibit a stable photocurrent of 180 μA, which is a 4-fold increase with respect to that of the Sn₃O₄ nanoflakes on carbon paper, and a two-order increase with respect to that of the TiO₂ NRs arrays. The evolution of hydrogen according to the photo-catalytic water-splitting process showed that Sn₃O₄/TiO₂ heterostructures have a good photocatalytic hydrogen evolution activity with the rate of 5.23 μmol h⁻¹, which is significantly larger than that of Sn₃O₄ nanoflakes (0.40 μmol h⁻¹) and TiO₂ nanorods (1.13 μmol h⁻¹). Furthermore, the mechanism behind this was discussed. The detector has reproducible and flexible properties, as well as an enhanced photosensitive performance.

Received 23rd May 2019

Accepted 19th July 2019

DOI: 10.1039/c9ra03885j

rsc.li/rsc-advances

Introduction

TiO₂, as one of the widest band gap semiconductors (~3.0 eV), is widely used in photocatalysts and photoelectrodes due to its strong optical absorption, favorable band edge positions, and abundant availability.¹ For example, oriented, single-crystalline rutile TiO₂ nanorod films on transparent conductive fluorine-doped tin oxide (FTO) substrates or carbon fiber were used as dye-sensitized solar cells (DSSCs) and exhibited an improved cell performance due to a direct connection of the point of photo-generation with the collection electrode.^{2,3} However, the energy unitization efficiency of TiO₂ is limited because of its wide band gap and the rapid recombination of photogenerated electron-hole pairs. Metal/nonmetal element doping or decoration was developed to increase its photoactivity, for example, TiO₂ modification with carbon nanolayers used as a photocatalyst led to an enhanced efficiency due to the increased substrate adsorption in the vicinity of the photocatalytic sites and high migration efficiency of photoinduced electrons at the carbon/TiO₂ interface.^{4,5} And metal modification of TiO₂ to increase photocatalytic properties of nanoparticles were reported also.^{6,7}

Among their methods, heterogeneous photocatalysts were regarded as an effective way to improve photocatalytic activity,

since heterojunctions can promote charge migration across both the semiconductor/electrolyte and the semiconductor/photoelectrode interface effectively separating photogenerated electrons and holes.⁸⁻¹⁰ P-SnO/*n*-TiO₂ composite electrodes revealed a better PEC performance as reported by Naeem *et al.*¹¹ And tree-like TiO₂ architectures assembled with CdS and reduced graphene oxide can improve photoelectrochemical performance as reported by Pathak *et al.*¹²

On the other hand, a mixed-valence tin oxide (Sn²⁺ and Sn⁴⁺) has a strong resistance against acidic/alkaline solutions and exhibits a good photocatalytic activity without generating secondary pollutants under irradiation with visible light. It is a desirable material for PEC-type photodetectors and an efficient visible-light-driven photocatalyst.¹³⁻¹⁶ To improve the photoelectric properties, Sn₃O₄ nanomaterials combined with others have been used as electrodes and photocatalysts. For example, integrated Sn₃O₄ nanosheets and rGO nanosheets as hybrid nanostructures were used as high-performance photocatalysts.¹⁷ With the combination of visible light active Sn₃O₄ and ultraviolet (UV) light active TiO₂, this composite can be a broad spectrum photocatalytic material from the UV to visible region as well as having enhanced separation of photogenerated electrons and holes,¹⁸ therefore people paid more attention to TiO₂@Sn₃O₄ nanostructures. For example, 3D lupinus-like TiO₂@Sn₃O₄ nanostructures on a transparent F-doped SnO₂ (FTO) glass substrate were prepared and used as photoanode for PEC water splitting as reported by Zhu *et al.*¹⁹ TiO₂@Sn₃O₄ hybrid nanobelts exhibited markedly enhanced photoelectrochemical (PEC) response, which caused higher

^aCollege of Physics Science and Technology, Institute of Optoelectronic Technology, Yangzhou University, Yangzhou 225002, P. R. China. E-mail: xhzeng@yzu.edu.cn; wwxia@yzu.edu.cn

^bCollege of Electrical, Energy and Power Engineering, Yangzhou 225127, P. R. China

[†] W. X. and H. Q. contributed equally to this work.



photocatalytic hydrogen evolution even without the assistance of Pt as a co-catalyst, and enhanced the degradation ability of organic pollutants under both UV and visible light irradiation.²⁰

Recently, self-powered photodetectors (SPPD) are becoming a promising candidate for application in high-sensitivity and high-speed SPPDs because they do not require batteries as an external power source.^{21,22} For example, TiO₂ based self-powered photochemical UV detectors have been reported, but they are restricted to UV light.^{23–25} To better use solar light for energy conversion, it is very important to extend the spectrum to the visible region. Although there are some discussions on the TiO₂@Sn₃O₄ electrodes, flexible SPPDs based on TiO₂@Sn₃O₄ haven't been reported yet.

Herein, TiO₂ nanorod arrays (NRs) vertically aligned on the carbon fiber papers were synthesized *via* a hydrothermal route, where TiO₂ nanorods have a diameter of about 500–1000 nm; then Sn₃O₄ nanoflakes (NFs) with a thickness of less than 100 nm and width of 100–300 nm were grown on the surface of TiO₂ nanorod. Furthermore, hybrid PEC-type photodetectors were designed using three prepared 3-D (three dimensional) hierarchical arrays, TiO₂, Sn₃O₄ and TiO₂@Sn₃O₄ as photoanodes, respectively. As a visible light SPPD device, TiO₂@Sn₃O₄ heterostructures exhibit a stable photocurrent of 180 μA, which is a 4-fold increase with respect to that of Sn₃O₄ NFs on carbon paper, and a two-order increase with respect to that of TiO₂ NRs on carbon paper. The detector exhibits reproducible and flexible properties, as well as an enhanced photosensitive performance. Finally, the photocatalytic properties of the pure Sn₃O₄, TiO₂ NRs and their combinations have been studied, where the evolution of hydrogen was measured according to the photocatalytic water-splitting process. The results show that Sn₃O₄/TiO₂ heterostructures have hydrogen evolution activity with the rate of 5.23 μmol h⁻¹, significantly larger than that of others. The mechanism behind has been discussed.

Experimental section

Materials

All chemicals were analytical-grade and used without further purification. Titanium butoxide (Ti(OC₄H₉)₄), tin dichloride dehydrate (SnCl₂·2H₂O), sodium citrate dihydrate (Na₃C₆H₅O₇·2H₂O, 99%), ethanol, and hydrochloric acid (HCl, 36.5–38% by weight) were purchased from Sinopharm Chemical Reagent Co., Ltd. Commercial carbon fiber papers were provided by FuelCellStore.

Synthesis of TiO₂ NRs

TiO₂ nanorod arrays (NRs) were prepared on the carbon fiber papers by the one-step hydrothermal method. Firstly, the commercial carbon fiber papers were cut into the desired sizes and ultrasonically washed using deionized water and ethanol. Then, 12 mL of deionized water was mixed with 12 mL of hydrogen chloride (36.5–38% by weight). The mixture was stirred for 5 min before the addition of 400 μL of titanium butoxide (97% Aldrich). After stirring for another 5 min, the mixture was transferred into a 50 mL Teflon-lined stainless steel autoclave

with the treated carbon fiber paper vertically immersed in the reaction solution. The hydrothermal reaction was carried out at 180 °C for 18 h and cooled naturally to room temperature. Finally, the carbon fiber paper substrates covered by TiO₂ NRs were washed with deionized water.

Synthesis of Sn₃O₄ NFs

Sn₃O₄ nanoflakes (NFs) were prepared on the carbon fiber papers by a modified hydrothermal approach, which is similar to the reported in our previous study.²⁶ In detail, 1.073 g of SnCl₂·2H₂O and 2.940 g Na₃C₆H₅O₇·2H₂O were dissolved in the mixture of 20 mL de-ionized water and 20 mL alcohol under constant magnetic stirring for approximately 60 min. The obtained homogeneous solution was transferred into a Teflon liner of 50 mL capacity with the carbon fiber paper vertical immersed into the reaction solution and keeping sealed under 180 °C for 18 h. After the reaction, the carbon fiber paper coated with a brown product was further washed with deionized water and absolute ethanol for several times. The final sample dried in an oven before characterization.

Synthesis of TiO₂@Sn₃O₄ hierarchical heterostructured arrays

Details of growth process of the TiO₂@Sn₃O₄ hierarchical heterostructured arrays were described previously. 0.35 g of SnCl₂·2H₂O and 1.14 g of Na₃C₆H₅O₇·2H₂O were dissolved in a mixture of 25 mL of deionized water and 25 mL of alcohol under constant magnetic stirring for approximately 60 min. Then, the mixture was transferred to a Teflon-lined autoclave (50 mL). Subsequently, the carbon fiber paper covered by TiO₂ NRs was vertically immersed into the aforementioned mixture. The hydrothermal reaction was carried out at 180 °C for 18 h and cooled naturally to room temperature. Finally, the resulting carbon fiber papers with TiO₂@Sn₃O₄ hierarchical heterostructured arrays were rinsed with deionized water and dried at 60 °C in air.

Characterization

The morphology and microstructure of the TiO₂@Sn₃O₄ heterostructured nanowire arrays on carbon fiber papers were examined by a Hitachi S-4800 field emission scanning electron microscope (FESEM) and a Tecnai G2 F30 field emission transmission electron microscope (TEM) operated at an accelerating voltage of 300 kV. The phase and composition of samples were analyzed by powder X-ray diffraction (XRD, Bruker D8 advance) with Cu Kα (λ = 1.5406 Å). UV-visible absorption spectra (200–1200 nm) were measured using a Varian Cary 50 UV-visible spectrophotometer. X-ray photoelectron spectroscopy (XPS) was conducted on an ESCALAB-250Xi photoelectron spectroscopy to obtain information on the valence state of the Ti and O ions.

PEC measurements

To perform the PEC tests, the Zanner CIMPS electrochemical workstation (Germany) was used to examine the photocurrent densities' curves and electrochemical impedance spectroscopy



(EIS) plots in a three-electrode mode. PEC measurements were performed in 0.1 M Na₂SO₄ using Pt wire as the counter electrode and Ag/AgCl in saturated KCl as a reference electrode. The carbon fiber papers with TiO₂@Sn₃O₄ hierarchical heterostructured arrays were acted as the working electrode and placed in the cell with an area of 1 × 1 cm² exposed to the electrolyte. A 500 W Xe lamp (CEL-HXF 300, Beijing Au-light, China) was employed as incident light source to study the PEC response of the samples. The H₂ evolution experiments were carried out in a gas-closed circulation system under a 300 W Xe lamp.

Results and discussion

Morphology and structure

The schematic diagram of the formation process of the TiO₂@Sn₃O₄ hierarchical heterostructured nanowire arrays on carbon fiber papers is shown in Fig. 1a, which involves two major steps. In the first step, large-scale well-aligned TiO₂ nanowires are grown on the carbon fiber papers by the one-step hydrothermal method. High-density TiO₂ NRs are grown uniformly on the carbon fiber papers, which also serve as stems to provide a platform for later Sn₃O₄ NFs growth. In the second step, the Sn₃O₄ NFs were conformably coated onto TiO₂ nanowire stems by a facile and effective hydrothermal method. Fig. 1b reveals the crystal structure of the as-synthesized TiO₂, Sn₃O₄ and TiO₂@Sn₃O₄ nanowires heterostructure arrays on carbon fiber papers. The diffraction peaks in each pattern at 26.22° and 54.72° are indexed to the carbon fiber paper substrate. For TiO₂ NRs on the carbon fiber paper substrate, the diffraction peaks at 2θ values of 27.45°, 36.08°, 41.22°, 44.05°, 56.64°, 62.74°, 64.04°, 69.01° and 69.79° can be well identified as (110), (101), (111), (210), (220), (002), (310), (301) and (112) planes of the tetragonal rutile TiO₂ phase (JCPDS 21-1276). Diffraction peaks at about 33.01°, 37.07° and 51.69° can be indexed to (210), (130) and ($\bar{1}\bar{3}2$) phases of Sn₃O₄ (JCPDS 16-0737). Besides, the XRD pattern of as-synthesized TiO₂@Sn₃O₄ hierarchical nanowire arrays on carbon fiber papers is also shown in Fig. 1c. All the major diffraction peaks of TiO₂ and

Sn₃O₄ can also be identified in the pattern of TiO₂@Sn₃O₄ hierarchical structure and no extra peak was detected.

To observe the morphology and microstructure of the samples, the FESEM images of TiO₂ NRs and TiO₂@Sn₃O₄ hierarchical structure are shown in Fig. 2. Fig. 2a–c show FESEM images of TiO₂ NRs on carbon fiber paper substrate with different magnifications. With the hydrothermal synthesis, TiO₂ NRs with a size of 500–1000 nm grow vertically along the surface of the carbon fiber paper substrate forming nanowire arrays with good uniformity, each TiO₂ NR has a square shape. After the growth of Sn₃O₄ nanoflake branches by the followed hydrothermal method, it can be obviously noted that high-density secondary Sn₃O₄ nanoflake branches are successfully grown on the surface of the TiO₂ nanowires with good uniformity, which lead to a thicker and rougher surface of TiO₂ nanowires. The magnified image (Fig. 2f) reveals that Sn₃O₄ NFs have a thickness of less than 100 nm and width of 100–300 nm. Because of the existence of convenient diffusion pathways, these TiO₂@Sn₃O₄ nanowire array hierarchical structures are extraordinarily accessible to electrolytes during the electrochemical measurement process. In addition, the compact nanoflakes interlaced with each other can also greatly increase the capture of light. Further morphological and structural characterizations of the TiO₂@Sn₃O₄ hierarchical structure are performed using HRTEM. The low-magnification TEM image (Fig. 3a) reveals the typical heterostructured nanowire taken from hierarchical TiO₂@Sn₃O₄ nanowire arrays, which can be evidently observed that the individual TiO₂ nanowire with a length of several micrometers is covered by compact Sn₃O₄ nanoflake branches. A close examination of the exposed profile (inset of Fig. 3a) reveals that thickness of the outer Sn₃O₄ NFs is around several tens nm. The high resolution TEM examination shown in Fig. 3b reveals a distinct set of visible lattice fringes of 0.33 nm, corresponding to the (111) plane of triclinic Sn₃O₄ (JCPDS 16-0737). To determine the atomic distribution in TiO₂@Sn₃O₄ hierarchical structure, EDS element mapping analysis of the individual hybrid nanowire was performed (Fig. 3c–f), Ti, Sn and O elements are found clearly in the hierarchical heterostructure of TiO₂@Sn₃O₄ nanowire.

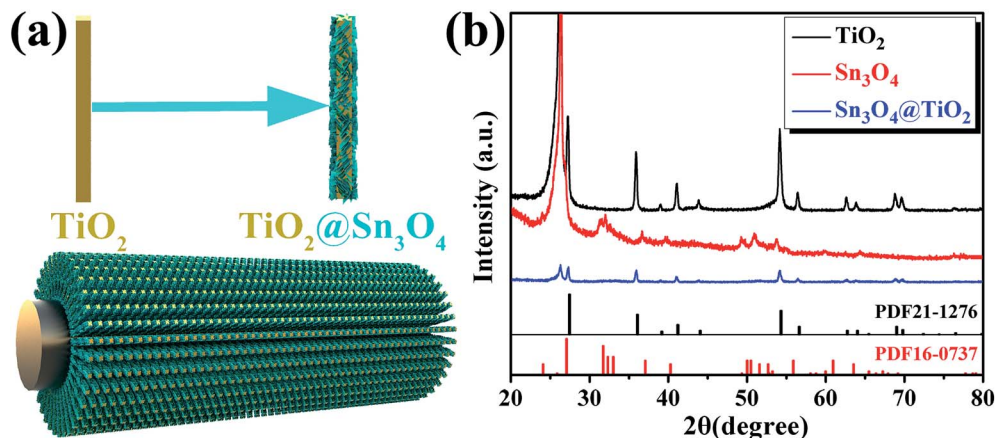


Fig. 1 (a) Schematic of fabrication process and (b) XRD patterns of TiO₂ NRs, Sn₃O₄ NFs and TiO₂@Sn₃O₄ heterostructure arrays grown on carbon fiber papers.



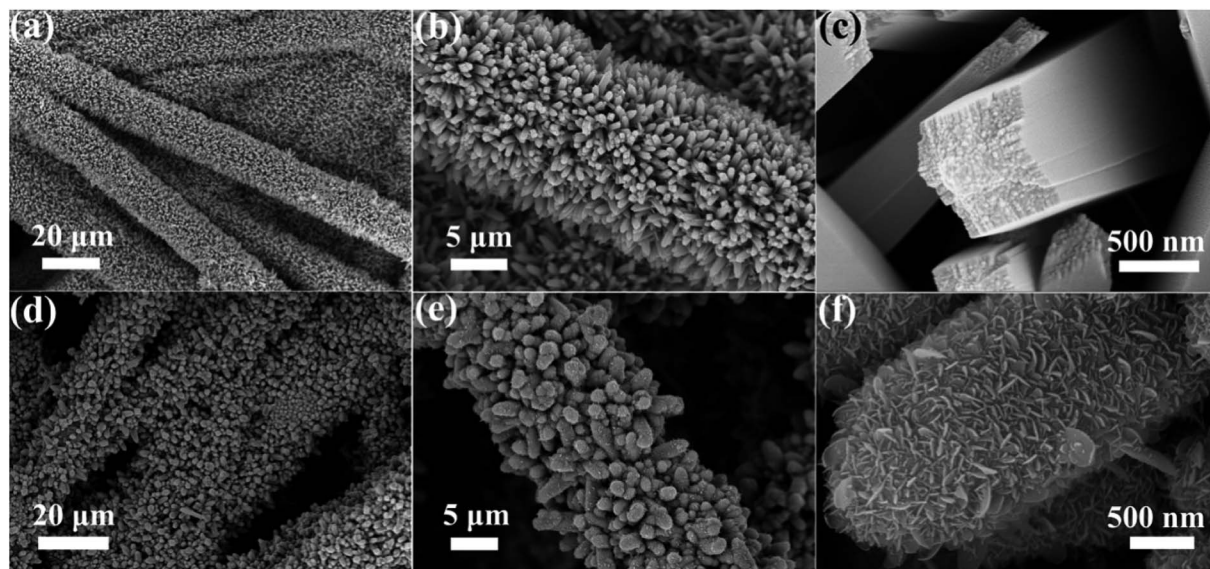


Fig. 2 FESEM images of (a–c) TiO_2 NRs and (d–f) $\text{TiO}_2@\text{Sn}_3\text{O}_4$ hierarchical structure grown on carbon fiber paper.

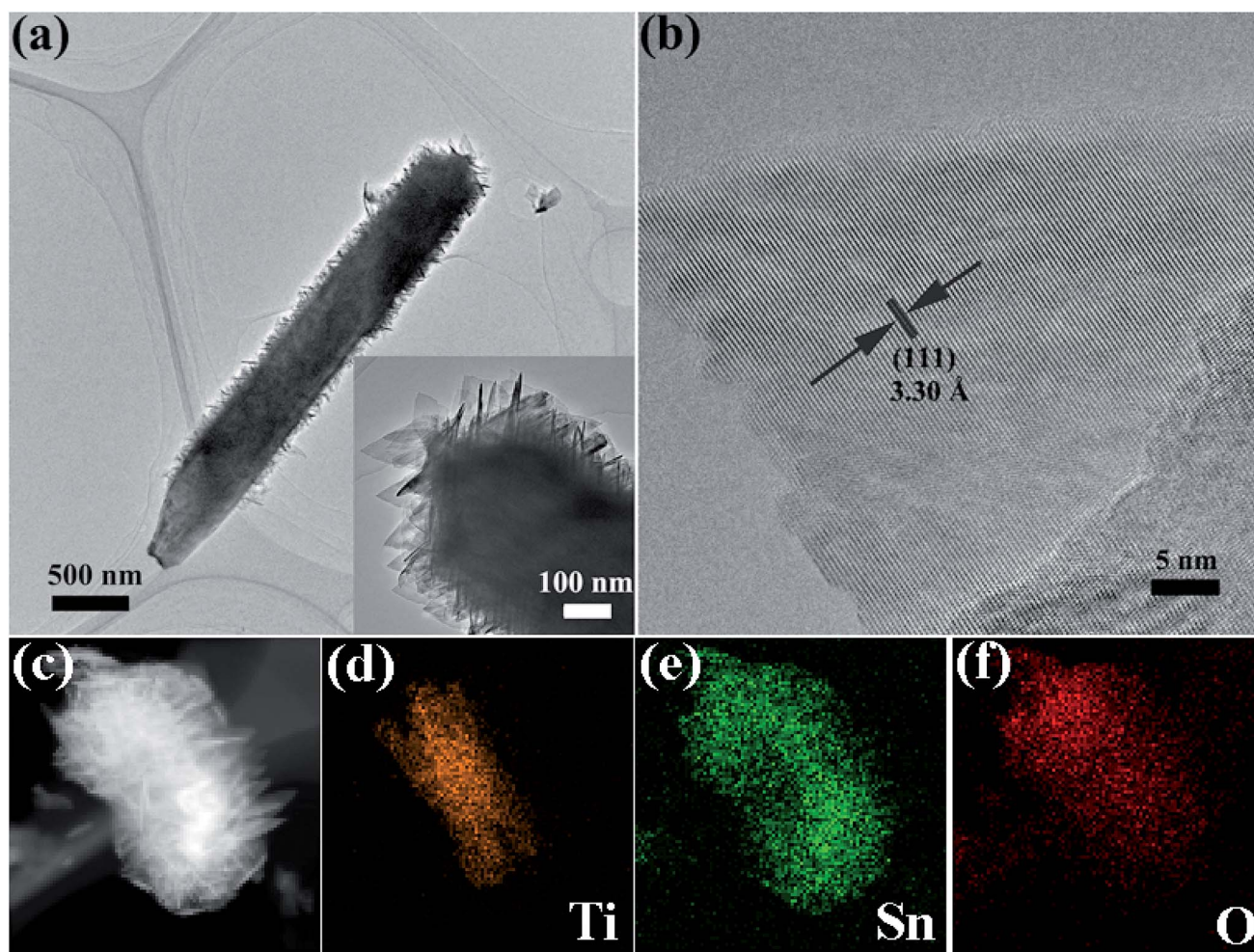


Fig. 3 TEM image (a) and HRTEM image (b) of a representative $\text{TiO}_2@\text{Sn}_3\text{O}_4$ heterostructured nanowire. (c–f) Elemental mapping images of an individual hybrid nanowire.



Optical properties of the as-prepared TiO₂ NRs, Sn₃O₄ NFs and TiO₂@Sn₃O₄ hierarchical structure grown on carbon fiber paper were investigated by diffuse reflectance UV-vis spectra (ultraviolet-visible spectroscopy) (Fig. 4a). Compared with bare TiO₂ NRs, TiO₂@Sn₃O₄ hierarchical structure shows significantly increased light absorption in the visible-light region. The absorption edge of the TiO₂ NRs (black line) is located at 408 nm, which indicates the energy gap is 3.04 eV. The absorption band edge of the Sn₃O₄ NFs (red) is closed to 435 nm (with the energy gap of 2.85 eV), which can absorb the visible light. For the 3D TiO₂@Sn₃O₄ hierarchical structure (blue line), its absorption band edge is at ~558 nm, showing a significant redshift compared with the bare TiO₂ NRs. Therefore, coupling TiO₂ NRs with Sn₃O₄ NFs can significantly broaden the range of photo-response, which can result in an enhancement of utilization of solar light and improved PEC performance. XPS measurements were used to investigate the surface composition of the as-synthesized products. Fig. 4b shows the XPS survey spectra of Sn₃O₄ NFs and TiO₂@Sn₃O₄ hierarchical structure. Chemical state binding energy of Sn 3d in the Sn₃O₄ NFs and TiO₂@Sn₃O₄ hierarchical structure was carried by XPS measurements as shown in Fig. 4c. Consistent with our previous study, the binding energies of Sn 3d_{3/2} and Sn 3d_{5/2} peaks in the pure Sn₃O₄ NFs locate at 494.64 eV and 486.15 eV, respectively. After growing onto the TiO₂ NRs, however, the Sn 3d_{3/2} and Sn 3d_{5/2} peaks of TiO₂@Sn₃O₄ hierarchical structure obviously shifted to higher binding energies by 0.46 and 0.47 eV, respectively. Therefore, the observed peak shift indicates that the electrons are injected from Sn₃O₄ NFs to the TiO₂ NRs in TiO₂@Sn₃O₄ hierarchical structure. This result can be

Table 1 Energy level

Samples	E_g (eV)	E_C (eV) vs. vacuum)	E_F (eV) vs. vacuum)	E_V (eV) vs. vacuum)
TiO ₂	3.04	4.43	5.20	7.47
Sn ₃ O ₄	2.85	3.7	3.9	6.55

further supported by the shift by 0.4 eV of the Ti 2p_{3/2} peak in Fig. 4d. The TiO₂@Sn₃O₄ hierarchical structure is possibly advantageous because of their electronic band structure.

UPS measurements were carried out to study the surface electron behavior of TiO₂ NRs, as shown in Fig. 4e and f. Fig. 4e is a view of the secondary electron edge (SEE) energy corresponding to the left spectra in UPS data. The work function (ϕ) can be by observing the low energy secondary electron cutoff, which is ~5.20 eV for TiO₂ NRs. Fig. 4f is a view of the valence band maximum (VBM) region corresponding to the right spectra in UPS data and the VBM can be extracted from the Fig. 4f, which is about 2.2 eV for TiO₂ NRs. The energy band of Sn₃O₄ NFs has been discussed previously.²² Then, the conduction band and valence band (vs. vacuum) of TiO₂ NRs and Sn₃O₄ NF scan be obtained, as shown in Table 1.

The PEC measurements were carried out in a three-electrode configuration in 0.1 M Na₂SO₄ using Pt wire as a counter electrode, Ag/AgCl in saturated KCl as a reference electrode, and carbon-paper-supported Sn₃O₄ NFs, TiO₂ NRs and TiO₂@Sn₃O₄ hierarchical structures as active photoanodes, respectively, as shown in the Fig. 5a. The incident radiation is switched with an on/off interval of 20 s. Twenty repeated cycles are displayed in

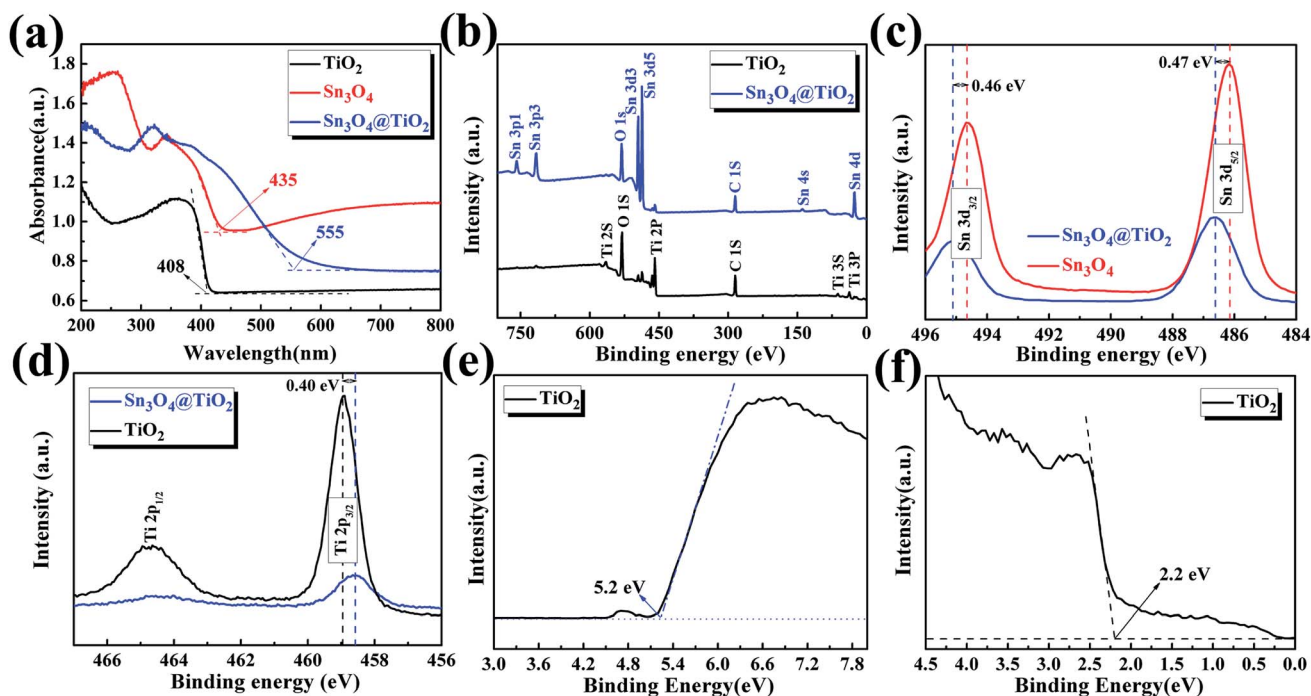


Fig. 4 (a) UV-vis spectra of the TiO₂ NRs and TiO₂@Sn₃O₄ hierarchical structure. (b) Survey XPS spectra of TiO₂ NRs and TiO₂@Sn₃O₄. (c) XPS spectra of Sn 3d for Sn₃O₄ NFs and TiO₂@Sn₃O₄. (d) XPS spectra of Ti 2p for Sn₃O₄ NFs and TiO₂@Sn₃O₄. (e) UPS secondary edge spectrum and (f) view of the valence band maximum (VBM) region.



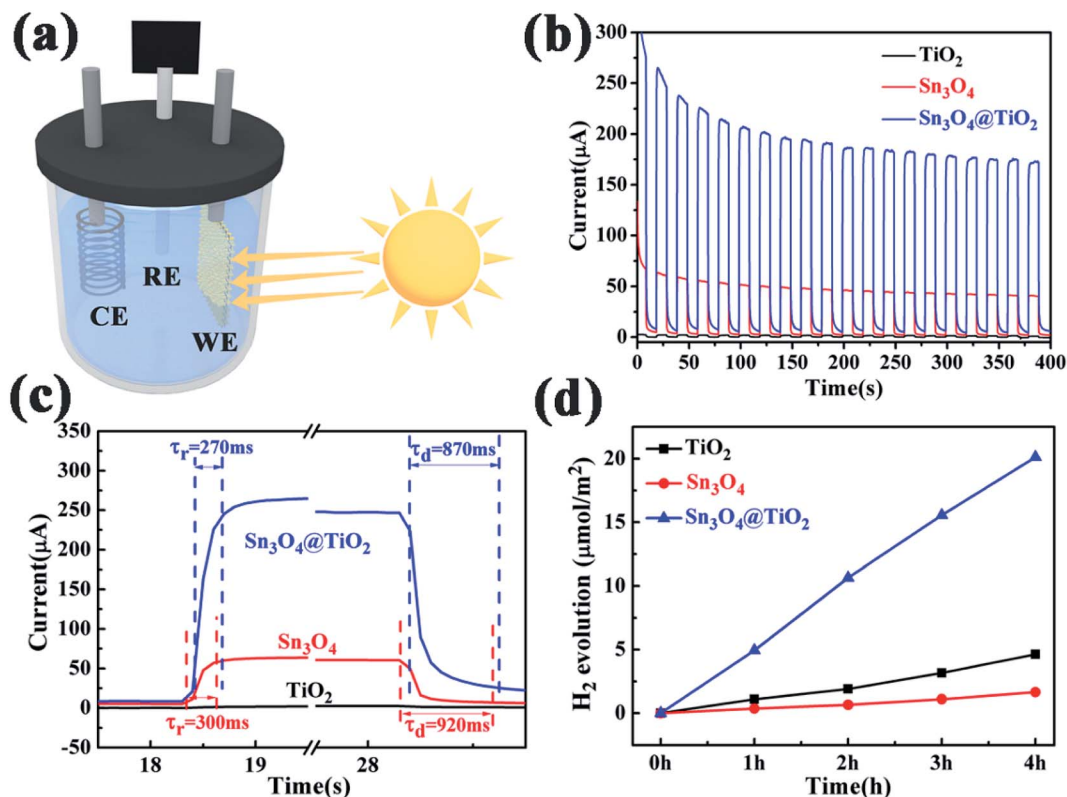


Fig. 5 (a) Schematic illustration of self-powered PEC type detector; (b) photocurrent responses under on/off of 20 s for 20 cycles at 0.0 V versus Ag/AgCl with illumination of 500 W Xe lamp; (c) enlarged rising and decaying edges of the photocurrent response; (d) H_2 evolutions as a function of time under irradiation of the 500 W Xe arc lamp.

Fig. 5b, in which TiO_2 NRs display a quite weak photocurrent under visible-light irradiation. The as-obtained Sn_3O_4 NFs exhibit a much enhanced photocurrent density of $\sim 40 \mu\text{A cm}^{-2}$ in the visible-light spectral region. However, the photocurrent exhibited nearly 40% decrease after 20 cycles. The $\text{TiO}_2@\text{Sn}_3\text{O}_4$ hierarchical electrode shows the highest photocurrent and a decrease of 30% compared with the initial photocurrent. From the magnified rising and decaying edges of photocurrent shown in Fig. 5c, a fast photo-response can be seen clearly. The rising time (τ_r , defined as the time to increase from 10% to 90% of the maximum photocurrent) and the decaying time (τ_d , defined as the time to recover from 90% to 10% of the maximum photocurrent) of $\text{TiO}_2@\text{Sn}_3\text{O}_4$ hierarchical electrodes are about 0.27 s and 0.87 s, respectively, faster than 0.30 s and 0.92 s for Sn_3O_4 NFs. The mechanism of reason for enhanced PEC performance will be explained in detail later. PEC measurements that the 3D $\text{TiO}_2@\text{Sn}_3\text{O}_4$ photoelectrode exhibited a stable photocurrent of $180 \mu\text{A}$, which is 4-fold increase with respect to that of Sn_3O_4 NFs, and two-order increase respect to that of TiO_2 NRs. In comparison to the report of ref. 19, the formation of the heterostructure on the photocurrent is much larger without external power source.

Furthermore, the photocatalytic property of the pure Sn_3O_4 , TiO_2 NRs and their combinations have been studied under visible light, where the evolution of hydrogen was measured according to the photo-catalytic water-splitting process, as shown in Fig. 5d. The results show that Sn_3O_4 NFs show

negligible photocatalytic hydrogen evolution activity with the rate of $0.40 \mu\text{mol h}^{-1} \text{cm}^{-2}$ and the rate of the TiO_2 NRs is $1.13 \mu\text{mol h}^{-1} \text{cm}^{-2}$, which is much lower than that of $\text{Sn}_3\text{O}_4/\text{TiO}_2$ heterostructures of $5.23 \mu\text{mol h}^{-1} \text{cm}^{-2}$, this value is comparable with the results reported by Kodiyath *et al.*²⁷ Contrary to the photocurrents, the H_2 generation of Sn_3O_4 is less than that of TiO_2 . Several aspects, such as the density of the photoanode catalysts, electron transportation and carrier's concentration *etc.*, will influence the H_2 generation. In the further work we will study them.

To further understand the reasons of the charge transfer process occurring at the interface of photoelectrode/electrolyte, electrochemical impedance spectroscopy (EIS)^{28,29} was carried out and presented in Fig. 6a and b. The equivalent RC circuit was used to interpret the EIS results (see inset of Fig. 6b). As shown in Fig. 6a and b, each Nyquist plots are composed of one semicircle and a slope line. For deeper analysis, all Nyquist plots display a semicircle at high frequencies whose diameter represents the charge-transfer resistance (R_{ct}), which reflects the electron transfer kinetics of the redox probe at the interface. The slope line at low frequency is related to the diffusion process. The corresponding equivalent circuit is depicted in the inset of Fig. 6b, where R_s denotes the series resistance at the interface of the photoelectrode material and the carbon fiber paper substrate, C_{dl} reflects the constant phase element that models capacitance of the double layer, and Z_w stands for the Warburg impedance originated from the diffusion process at



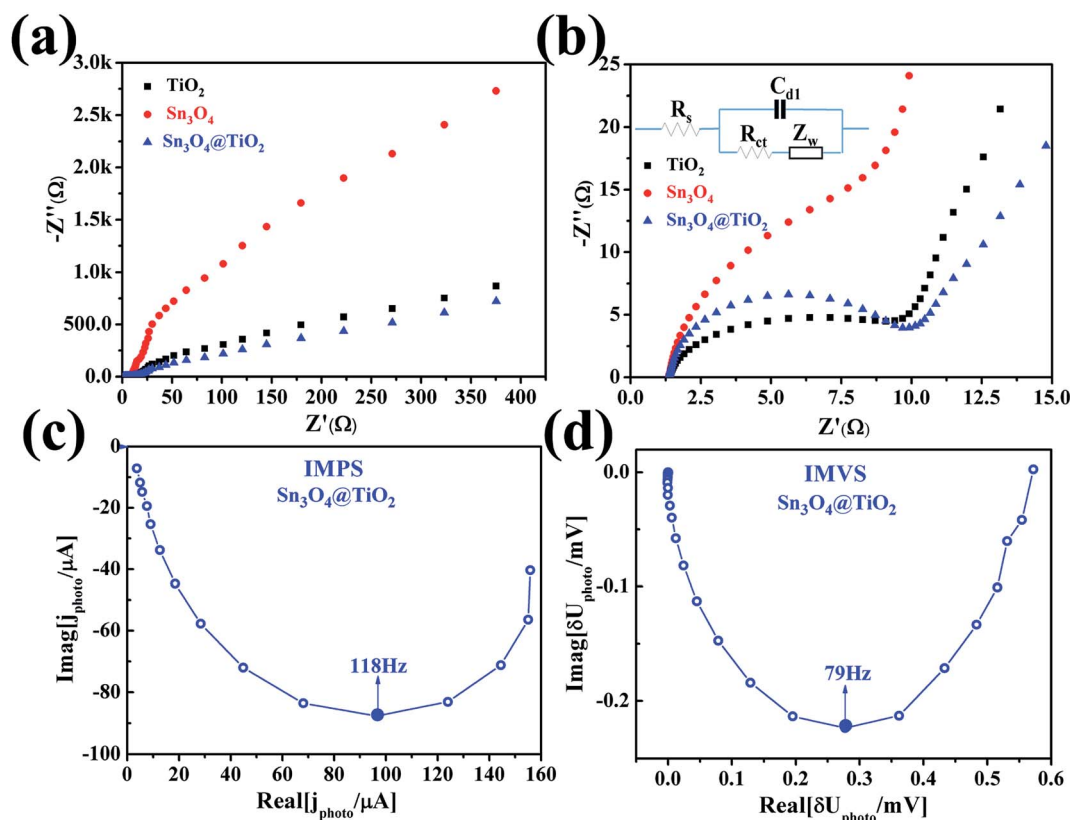


Fig. 6 (a) Nyquist plots of TiO_2 NRs, Sn_3O_4 NFs and $\text{TiO}_2@Sn_3O_4$ heterostructure arrays grown on carbon fiber papers; (b) plots in the expanded high-frequency region and the inset represents the equivalent circuit applied to fit the impedance data; (c) typical IMPS and (d) IMVS plot of $\text{TiO}_2@Sn_3O_4$ heterostructure arrays.

the electrode surface. After being decorated with Sn_3O_4 NFs, the value R_{ct} of $\text{TiO}_2@Sn_3O_4$ hierarchical photoelectrode is almost the same, which is smaller than the corresponding value of Sn_3O_4 NFs. The above result demonstrates that TiO_2 NRs provide a conduction path and rapidly transfer the photoelectrons coming from Sn_3O_4 NFs to the carbon fiber paper substrate along the vertically oriented TiO_2 NRs, which is also correlated to the enhanced PEC performance. To obtain deep insights into the enhanced PEC properties of the $\text{TiO}_2@Sn_3O_4$ hierarchical electrodes, intensity modulated photocurrent spectroscopy (IMPS) and intensity modulated photovoltage spectroscopy (IMVS) have been employed to investigate further the electron transport and recombination process, as shown in Fig. 6c and d. The IMPS and IMVS plots display a semicircle in the complex plane under the incident light source was an LED with a wavelength of 564 ± 60 nm. From the IMPS measurement (Fig. 6c), the transport time (τ_d) of injected electrons from Sn_3O_4 NFs to TiO_2 NRs can be calculated from the following equation:

$$\tau_d = 1/(2\pi f_{d,\min}),$$

where $f_{d,\min}$ is characteristic frequency at the minimum of the IMPS imaginary component. Thus, τ_d value is estimated to be 1.35 ms. In addition, from the IMVS measurement (Fig. 6d), the recombination lifetime (τ_n) was determined using the following equation:

$$\tau_n = 1/(2\pi f_{n,\min}),$$

where $f_{n,\min}$ is the characteristic frequency at the minimum of IMVS imaginary component. The τ_n can be calculated to be 2.0 ms for $\text{TiO}_2@Sn_3O_4$ hierarchical photoelectrode. All the above results indicate that vertically oriented TiO_2 NRs can serve as fast electron transport and $\text{TiO}_2@Sn_3O_4$ heterostructure can increase electron lifetime and result in the enhanced PEC performance.

Based on the above measurements and analyses, by combining both the band gap estimated from optical absorption and the conduction band and valence band (vs. vacuum) obtained by UPS, the energy band alignment of TiO_2 NRs and Sn_3O_4 NFs is displayed in Fig. 7a. When Sn_3O_4 NFs contact with TiO_2 NRs to form a heterojunction, the band structure of $\text{TiO}_2@Sn_3O_4$ is reconfigured. The bandgap energy of Sn_3O_4 (2.85 eV) is smaller than TiO_2 (3.04 eV) and both the potentials of VB and CB of Sn_3O_4 are higher than those of TiO_2 , so $\text{TiO}_2@Sn_3O_4$ heterostructure belongs to a typical type-II heterojunction. Under visible-light irradiation, photogenerated holes and electrons appear in the VB and CB of Sn_3O_4 NFs. Due to type-II heterostructure, the photogenerated electrons in Sn_3O_4 CB were easily injected into the TiO_2 CB. Effective separation of photoexcited electron-hole pairs could be accomplished by a longer electron lifetime. To explain the enhanced PEC performance of $\text{TiO}_2@Sn_3O_4$ photoelectrode in the visible-light



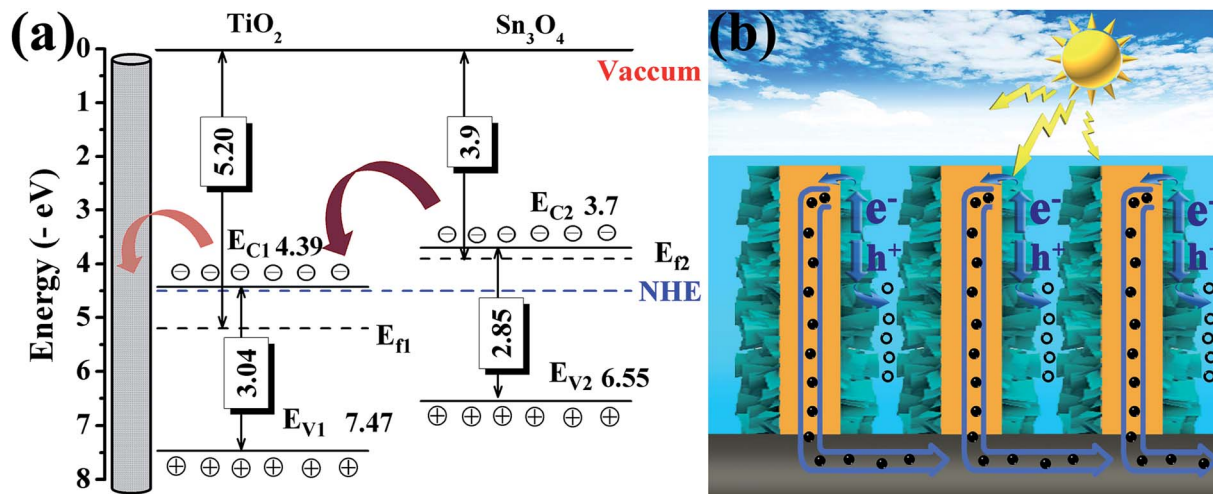


Fig. 7 (a) Proposed energy band alignment and (b) scheme of the electron–hole pair separation and the transfer process in $\text{TiO}_2@\text{Sn}_3\text{O}_4$ photoelectrode.

spectral region, we present the scheme of the electron–hole pair separation and the transfer process in $\text{TiO}_2@\text{Sn}_3\text{O}_4$ hierarchical photoelectrode (Fig. 7b). Generally, enhanced PEC performance of $\text{TiO}_2@\text{Sn}_3\text{O}_4$ photoelectrode may be attributed to the reasonable design of $\text{TiO}_2\text{NRs}@\text{Sn}_3\text{O}_4\text{NFs}$ heterostructure. On one hand, the aligned TiO_2 NRs can provide a conduction path and rapidly transfer electrons to carbon fiber paper substrate along the vertically oriented TiO_2 NRs. On the other hand, the type-II heterojunction of $\text{TiO}_2@\text{Sn}_3\text{O}_4$ heterostructure can drive photoexcited electron transfer from Sn_3O_4 NFs to TiO_2 NRs. In one word, for our $\text{TiO}_2@\text{Sn}_3\text{O}_4$ photoelectrode under the synergistic effects between unique band structures and morphology, which is crucial for the enhancement of PEC performance.

Conclusion

In this paper, $\text{TiO}_2@\text{Sn}_3\text{O}_4$ arrays vertically aligned on the carbon fiber papers were synthesized and used as photoanodes to improve the photocurrent performance under visible light. Because of the 3-D structure, the $\text{TiO}_2@\text{Sn}_3\text{O}_4$ arrays can absorb more incident lights which have been reflected among Sn_3O_4 NFs, at same time there are more interfacial states to adsorb electrolyte molecules. The $\text{TiO}_2@\text{Sn}_3\text{O}_4$ arrays not only extend the spectra from UV to visible region with respect to TiO_2 , but also increase the separation of photogenerated electrons and hole due to the good band alignment of type-II heterostructure for $\text{TiO}_2@\text{Sn}_3\text{O}_4$. Therefore, as photoanodes in self-powered photoelectrochemical cell-type (PEC) photodetector under visible light, $\text{TiO}_2@\text{Sn}_3\text{O}_4$ heterostructures exhibit a stable photocurrent of $180 \mu\text{A}$, which is 4-fold increase with respect to that of Sn_3O_4 NFs, and two-order increase respect to that of TiO_2 NRs arrays. $\text{Sn}_3\text{O}_4/\text{TiO}_2$ heterostructures also have a good photocatalytic hydrogen evolution activity with the rate of $5.23 \mu\text{mol h}^{-1}$, which is quite larger than that of Sn_3O_4 nanoflakes ($0.40 \mu\text{mol h}^{-1}$) and TiO_2 NRs ($1.13 \mu\text{mol h}^{-1}$). By the way, the detector exhibits reproducible and flexible properties, as well as

an enhanced photosensitive performance. The results will be helpful for the construction of hierarchical structures used in the PEC detectors.

Conflicts of interest

The authors declare no competing financial interest.

Acknowledgements

This work was supported by the National Key Research and Development Program of China (Grant No. 2017YFB0403101), the National Natural Science Foundation of China (Grant 61604127, 61474096).

References

- W. A. Gil, A. M. Mahadeo, S. C. Weon, G. K. Hyun, C. Min and S. J. Jum, Enhanced solar photoelectrochemical conversion efficiency of the hydrothermally-deposited TiO_2 nanorod arrays: Effects of the light trapping and optimum charge transfer, *Appl. Surf. Sci.*, 2018, **440**, 688–699.
- L. Bin and S. A. Eray, Growth of oriented single-crystalline rutile TiO_2 nanorods on transparent conducting substrates for dye-sensitized solar cells, *J. Am. Chem. Soc.*, 2009, **131**, 3985–3990.
- W. X. Guo, C. Xu, X. Wang, S. H. Wang, C. F. Pan, C. J. Lin and Z. L. Wang, Rectangular bunched rutile TiO_2 nanorod arrays grown on carbon fiber for dye-sensitized solar cells, *J. Am. Chem. Soc.*, 2012, **134**, 4437–4441.
- G. Q. Chang, Z. Cheng, R. Warren, G. X. Song, J. Y. Shen and L. W. Lin, Highly efficient photocatalysts for surface hybridization of TiO_2 nanofibers with carbon films, *ChemPlusChem*, 2015, **80**, 827–831.
- X. Cai, H. W. Wu, H. C. Hou, M. Peng, X. Yu and D. C. Zou, Dye-sensitized solar cells with vertically aligned TiO_2 nanowire arrays grown on carbon fibers, *ChemSusChem*, 2014, **7**, 474–482.



- 6 P. K. Sharma, M. A. L. R. M. Cortes, J. W. J. Hamiltona, Y. S. Han, J. A. Byrne and M. Nolan, Surface modification of TiO₂ with copper clusters for band gap narrowing, *Catal. Today*, 2019, **321–322**, 9–17.
- 7 Z. M. Zhao, J. Sun, G. J. Zhang and L. J. Bai, The study of microstructure, optical and photocatalytic properties of nanoparticles (NPs)-Cu/TiO₂ films deposited by magnetron sputtering, *J. Alloys Compd.*, 2015, **652**, 307–312.
- 8 H. Masai, T. Miyazaki, K. Mibu, Y. Takahashi and T. Fujiwara, Phase separation and the effect of SnO addition in TiO₂-precipitated glass-ceramics, *J. Eur. Ceram. Soc.*, 2015, **35**, 2139–2144.
- 9 L. X. Liu, G. C. Fan, J. R. Zhang and J. J. Zhu, Ultrasensitive cathode photoelectrochemical immunoassay based on TiO₂ photoanode-enhanced 3D Cu₂O nanowire array photocathode and signal amplification by biocatalytic precipitation, *Anal. Chim. Acta*, 2018, **1027**, 33–40.
- 10 G. D. Moon, J. B. Joo, I. Lee and Y. Yin, Decoration of size-tunable CuO nanodots on TiO₂ nanocrystals for noble metal-free photocatalytic H₂ production, *Nanoscale*, 2014, **6**, 12002–12008.
- 11 R. Naeem, M. A. Ehsan, A. Rehman, Z. H. Yamani, A. S. Hakeem and M. Mazhar, Single step aerosol assisted chemical vapor deposition of p–n Sn(II) oxide–Ti(IV) oxide nanocomposite thin film electrodes for investigation of photoelectrochemical properties, *New J. Chem.*, 2018, **42**, 5256–5266.
- 12 P. Pathak, S. Gupta, K. Grosulak, H. Imahori and V. Subramanian, Nature-inspired tree-like TiO₂ architecture: a 3D platform for the assembly of CdS and reduced graphene oxide for photoelectrochemical processes, *J. Phys. Chem. C*, 2015, **119**, 7543–7553.
- 13 O. M. Berengue, R. A. Simon, A. J. Chiquito, C. J. Dalmaschio, E. R. Leite, H. A. Guerreiro and F. E. G. Guimaraes, Semiconducting Sn₃O₄ nanobelts: growth and electronic structure, *J. Appl. Phys.*, 2010, **107**, 033717.
- 14 W. W. Xia, H. B. Wang, X. H. Zeng, J. Han, J. Zhu, M. Zhou and S. D. Wu, High-efficiency photocatalytic activity of type II SnO/Sn₃O₄ heterostructures via interfacial charge transfer, *CrystEngComm*, 2014, **16**, 6841–6847.
- 15 Y. H. He, D. Z. Li, J. Chen, Y. Shao, J. J. Xian, X. Z. Zheng and P. Wang, Sn₃O₄: a novel heterovalent-tin photocatalyst with hierarchical 3D nanostructures under visible light, *RSC Adv.*, 2014, **4**, 1266–1269.
- 16 H. Song, S. Y. Son, S. K. Kim and G. Y. Jung, A facile synthesis of hierarchical Sn₃O₄ nanostructures in an acidic aqueous solution and their strong visible light-driven photocatalytic activity, *Nano Res.*, 2015, **8**, 3553–3561.
- 17 X. Yu, Z. H. Zhao, N. Ren, J. Liu, D. H. Sun, L. H. Ding and H. Liu, Top or Bottom, Assembling modules determine the photocatalytic property of the sheet like nanostructured hybrid photocatalyst composed with Sn₃O₄ and rGO (GQD), *ACS Sustainable Chem. Eng.*, 2018, **6**, 11775–11782.
- 18 X. Yu, L. F. Wang, J. Zhang, W. B. Guo, Z. H. Zhao, Y. Qin, X. N. Mou, A. X. Li and H. Liu, Hierarchical hybrid nanostructures of Sn₃O₄ on N doped TiO₂ nanotubes with enhanced photocatalytic performance, *J. Mater. Chem. A*, 2015, **3**, 19129–19136.
- 19 L. P. Zhu, H. Lu, D. Hao, L. L. Wang, Z. H. Wu, L. J. Wang, P. Li and J. H. Ye, Three-dimensional lupinus-like TiO₂ nanorod@Sn₃O₄ nanosheet hierarchical heterostructured arrays as photoanode for enhanced photoelectrochemical performance, *ACS Appl. Mater. Interfaces*, 2017, **9**, 38537–38544.
- 20 G. H. Chen, S. Z. Ji, Y. H. Sang, S. J. Chang, Y. N. Wang, P. Hao, J. Claverie, H. Liu and G. W. Yu, Synthesis of scaly Sn₃O₄/TiO₂ nanobelt heterostructures for enhanced UV-visible light photocatalytic activity, *Nanoscale*, 2015, **7**, 3117.
- 21 W. J. Lee and M. H. Hon, An ultraviolet photo-detector based on TiO₂/water solid–liquid heterojunction, *Appl. Phys. Lett.*, 2011, **99**, 251102.
- 22 W. W. Xia, H. Y. Qian, X. H. Zeng, J. Dong, J. Wang and Q. Xu, Visible-light self-powered photodetector and recoverable photocatalyst fabricated from vertically aligned Sn₃O₄ nanoflakes on carbon paper, *J. Phys. Chem. C*, 2017, **121**, 19036–19043.
- 23 X. D. Li, C. T. Gao, H. G. Duan, B. G. Lu, X. J. Pan and E. Q. Xie, Nanocrystalline TiO₂ film based photoelectrochemical cell as self-powered UV-photodetector, *Nano Energy*, 2012, **1**, 640–645.
- 24 Z. R. Wang, S. H. Ran, B. Liu, D. Chen and G. Z. Shen, Multilayer TiO₂ nanorod cloth/nanorod array electrode for dye-sensitized solar cells and self-powered UV detectors, *Nanoscale*, 2012, **4**, 3350–3358.
- 25 C. T. Gao, X. D. Li, X. P. Zhu, L. L. Chen, Y. Q. Wang, F. Teng, Z. X. Zhang, H. G. Duan and E. Q. Xie, High performance, self-powered UV-photodetector based on ultrathin, transparent, SnO₂–TiO₂ core–shell electrodes, *J. Alloys Compd.*, 2014, **616**, 510–515.
- 26 W. W. Xia, H. Y. Qian, X. H. Zeng, J. Dong, J. Wang and Q. Xu, Visible-light self-powered photodetector and recoverable photocatalyst fabricated from vertically aligned Sn₃O₄ nanoflakes on carbon paper, *J. Phys. Chem. C*, 2017, **121**, 19036–19043.
- 27 R. Kodiyath, J. J. Wang, T. Hara, A. Dakshanamoorthy, S. Ishihara, K. Ariga, J. H. Ye, N. Umezawa, H. Abe, *et al.*, Photocatalytic water splitting under visible light by mixed-valence Sn₃O₄, *ACS Appl. Mater. Interfaces*, 2014, **6**, 3790–3793.
- 28 P. A. DeSario, J. J. Pietron, D. H. Taffa, R. Compton, S. Schünemann, R. Marschall, T. H. Brintlinger, R. M. Stroud, M. Wark, J. C. Owrutsky and D. R. Rolison, Correlating changes in electron lifetime and mobility on photocatalytic activity at network-modified TiO₂ aerogels, *J. Phys. Chem. C*, 2015, **119**, 17529–17538.
- 29 L. M. Peter and K. G. U. Wijayantha, Intensity dependence of the electron diffusion length in dye-sensitized nanocrystalline TiO₂ photovoltaic cells, *Electrochem. Commun.*, 1999, **1**, 576–580.

